

# Analyzing the Effects of Interconnect Parasitics in the STT CRAM In-Memory Computational Platform

MASOUD ZABIHI<sup>1</sup>, ARVIND K. SHARMA, MEGHNA G. MANKALALE<sup>1</sup>,  
ZAMSHED IQBAL CHOWDHURY<sup>1</sup> (Member, IEEE), ZHENGYANG ZHAO<sup>1</sup>,  
SALONIK RESCH, ULYA R. KARPUZCU, JIAN-PING WANG<sup>1</sup> (Fellow, IEEE),  
and SACHIN S. SAPATNEKAR<sup>1</sup> (Fellow, IEEE)

Department of Electrical and Computer Engineering, University of Minnesota, Minneapolis, MN 55455 USA  
CORRESPONDING AUTHOR: M. ZABIHI (zabih003@umn.edu)

This work was supported in part by NSF SPXunder Award CCF-1725420.

This article has supplementary downloadable material available at <http://ieeexplore.ieee.org>, provided by the authors.

**ABSTRACT** This article presents a method for analyzing the parasitic effects of interconnects on the performance of the STT-MTJ-based computational random access memory (CRAM) in-memory computation platform. The CRAM is a platform that makes a small reconfiguration to a standard spintronics-based memory array to enable logic operations within the array. The analytical method in this article develops a methodology that quantifies the way in which wire parasitics limit the size and configuration of a CRAM array and studies the impact of cell- and array-level design choices on the CRAM noise margin. Finally, the method determines the maximum allowable CRAM array size under various technology considerations.

**INDEX TERMS** In-memory computing, spin-transfer torque computational random access memory (STT-CRAM), spintronics.

## I. INTRODUCTION

HIGH energy and delay overheads for transferring data between processing and memory units have motivated intense interest in reducing the distance between memory and computation units. While near-memory computing places computational units at the periphery of memory for fast data access, true in-memory computing uses the memory array to perform computations through simple reconfiguration. True in-memory computing systems outperform near-memory and conventional computing systems because they massively reduce data communication energy and can provide high levels of parallelism. This article studies the impact of interconnect parasitics in the spin-transfer torque computational random access memory (STT-CRAM), a true in-memory processing platform [1]–[3]. Only a few prior works [4], [5] have attempted to incorporate the parasitic effects of interconnects in their analysis on in-memory computing, but their models did not consider all contributing factors based on realistic layout considerations.

The CRAM uses a small modification to the high-endurance MTJ-based [6] memory cell to enable true in-memory logic operations. In the CRAM, the segment resistances of wires that carry the current are significantly smaller than MTJ resistances. This can be falsely lead to this assumption that the interconnect parasitic effects are negligible. This article develops an analytical method based on the layout considerations, which is used to study the

effects of design parameters on parasitics and performance, in order to build a robust CRAM design. The method considers multiple contributing factors simultaneously, e.g., reducing the access transistor resistance can potentially enhance the performance, but it also increases the area of the array and increases interconnect lengths, which can harm performance. We use this methodology to determine an optimal size for CRAM subarray.

In Section II, we provide an overview of the STT-CRAM. We then motivate the problem in Section III. Next, in Section IV, we develop a layout model for the CRAM in a FinFET technology, considering both the cell level and array level while also specifying metal layer usage. We develop the models for the impact of parasitics in Section V, evaluate the results of our analysis in Section VI, and conclude in Section VII.

## II. OVERVIEW OF THE STT-CRAM

The core storage unit in an STT-CRAM is the STT-MTJ, which consists of a fixed layer, with a fixed magnetization orientation, and a free layer whose magnetization can be in one of the two possible states—parallel (P) and antiparallel (AP) [7]. The two states have different electrical resistances: the parallel state resistance  $R_P < R_{AP}$  and the AP state resistance. We denote the P and AP states as logic 0 and 1, respectively. The MTJ state can be altered by passing a critical current of magnitude  $I_c$  through it in the appropriate direction.

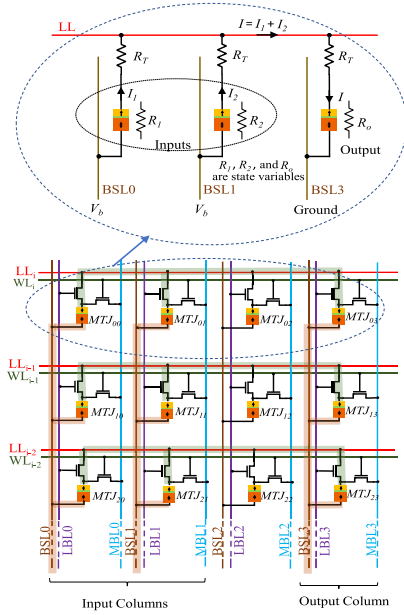


**FIGURE 1. Structure of STT-CRAM array, highlighting the current paths during a logic operation with two inputs and one output.**

Fig. 1 shows the structure of an STT-CRAM array, which uses a 2T1MTJ bit cell [1], [2], [8]. The configuration of the array is very similar to that of a standard 1T1MTJ STT-MRAM, and as in the case of the STT-MRAM, each bit cell is addressed using a memory wordline (WL). The additional transistor in the STT-CRAM is used for logic operations, and is turned ON by selecting the corresponding logic bitline (LBL).

The array can thus function in the memory or logic mode. In the memory mode, the transistor connected to WL is ON and read from (or write to) an MTJ is realized through memory bitline (MBL). Note that during the memory mode, the second transistor, which is connected to LBL, is OFF. In the logic mode, in the columns of the bit cells that correspond to inputs and the output, this LBL-connected transistor is turned ON. The access transistor connected to WL is OFF for all columns. This configuration allows the MTJs in the selected Bit cells in each row to be connected to a logic line (LL). By applying an appropriate voltage to the bit select lines (BSLs) of the input bit cells and grounding the BSL of the output, a state-dependent current, whose value depends on the resistance of MTJs and transistor resistance ( $R_T$ ), flows through the output MTJ. If this current exceeds  $I_c$ , the output state (the resistance of the output) is altered; otherwise, it remains the same.

Different logic functions can be realized in the STT-CRAM by altering two parameters [1], [2], [8]: 1) the bias voltage ( $V_b$ ) applied to the BSLs of the input MTJs and 2) the output preset state. In [2], for each gate, a range for  $V_b$  is calculated.

Next, we show how [2] derives an allowable range for  $V_b$  for a two-input AND gate, ignoring the parasitic effects of lines and transistors. An AND gate in each row can be realized by the configuration shown in the Top of Fig. 1, which highlights the path of current through the MTJs. Current  $I$  can be calculated by dividing  $V_b$  by the equivalent resistance  $((R_1 + R_T) || (R_2 + R_T)) + R_o$ , where “||” represents the

**TABLE 1. Bias voltage ranges and output preset values [2].**

Gate (Pre-set)	$V_{min} = \text{Minimum } V_b$	$V_{max} = \text{Maximum } V_b$
BUFFER(1)	$(R_A + R_B)I_c$	$2R_B I_c$
NOT(0)	$2R_A I_c$	$(R_A + R_B)I_c$
AND(1)	$(R_A    R_B + R_B)I_c$	$1.5R_B I_c$
NAND(0)	$(R_A    R_B + R_A)I_c$	$(0.5R_B + R_A)I_c$
OR(1)	$(0.5R_A + R_B)I_c$	$(R_A    R_B) + R_B)I_c$
NOR(0)	$1.5R_A I_c$	$(R_A    R_B + R_A)I_c$
MAJ3(1)	$(0.5R_A    R_B + R_B)I_c$	$(R_A    0.5R_B + R_B)I_c$
MAJ3(0)	$(0.5R_A    R_B + R_A)I_c$	$(R_A    0.5R_B + R_A)I_c$
MAJ5(1)	$((1/3)R_A    0.5R_B + R_B)I_c$	$(0.5R_A    (1/3)R_B + R_B)I_c$
MAJ5(0)	$((1/3)R_A    0.5R_B + R_A)I_c$	$(0.5R_P    (1/3)R_B + R_A)I_c$

equivalent resistance of parallel resistors. If  $R_A = R_P + R_T$  and  $R_B = R_{AP} + R_T$ , the current for each input state is

$$\begin{aligned} I_{00} &= V_b / (0.5R_A + R_B) & I_{11} &= 2V_b / (3R_B) \\ I_{01} &= I_{10} = V_b / ((R_A || R_B) + R_B). \end{aligned}$$

Since  $R_P < R_{AP}$ ,  $R_A < R_B$ , implying that

$$I_{11} < I_{01} = I_{10} < I_{00}. \quad (1)$$

The output MTJ is preset to logic 1. For an AND gate,  $I_{01} = I_{10} > I_c$ , switching the output state from 1 to 0. From (1)

$$V_b > (R_A || R_B + R_B)I_c. \quad (2)$$

On the other hand,  $V_b$  cannot be too large; if it is, the output is switched regardless of the states of inputs, i.e., we must ensure that  $I_{11}$  must not be larger than  $I_c$ , i.e., from (1)

$$V_b < 3R_B I_c / 2. \quad (3)$$

Considering these two constraints, we can present a bias voltage range for the AND gate. The voltage ranges and preset values for other logic functions can be obtained in a similar manner and are summarized in Table 1. The precise range of  $V_b$  is technology-dependent. To account for anticipated advances in spintronics [9], this article considers the MTJ specifications in today's technology and an advanced near-future technology [2]. In the rest of this article, we use today's and advanced MTJ parameters listed in Table 7 (see the Supplementary Material) for our calculations and evaluations.

### III. IMPACT OF WIRE PARASITICS

To show the impact of parasitics in a CRAM array, we consider a scenario where each row of the CRAM performs a BUFFER operation between Columns 1 and 10. The CRAM array can be built using either today's technology (today's CRAM) or using advanced technology (advanced CRAM). An electrical model of the current path is shown in Fig. 2; the bias voltage is applied between BSLs 1 and 10, and in each row, the current path goes through input and output MTJs, two access transistors, and a segment of LL. The model includes parasitic capacitances associated with each line segment and the transistor resistance. For the motivational example in Section III, built around Fig. 2, the transistors  $N_{fin}$  and  $N_{finger}$  are specific to the example and lead to the computed values of  $W_{cell}$  and  $L_{cell}$ . The remaining parameters are used throughout the rest of this article. The parameters used in the following motivational example are listed for both today's and advanced CRAMs in Table 2.

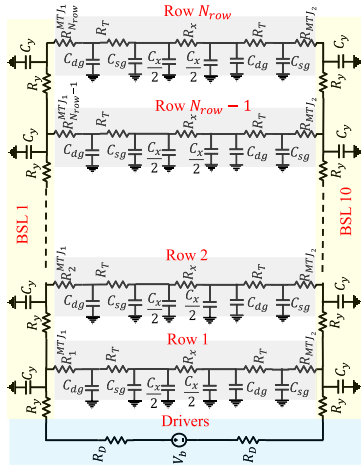


**FIGURE 2.** Circuit model of the current path for the implementation of BUFFER gates in CRAMs of various sizes.

**TABLE 2.** Parameters in the motivational example.

Parameter	Description	Today's CRAM	Advanced CRAM
$N_{fin}$	Number of fins	4	2
$N_{finger}$	Number of fingers	8	4
$W_{cell}$	Cell width	189nm	135nm
$L_{cell}$	Cell length	1323nm	675nm
$R_T$	Transistor resistance	0.178 $\Omega$	0.713 $\Omega$
$d_{column}$	Input-output distance	9	9
$R_x$	LL segment resistance	33.300 $\Omega$	25.100 $\Omega$
$R_y$	BSL segment resistance	0.026 $\Omega$	0.032 $\Omega$
$C_x$	LL segment capacitance	11.240fF	4.223fF
$C_y$	BSL segment capacitance	816aF	341aF
$C_{gd}$	Transistor g-d capacitance	320aF	320aF
$C_{sg}$	Transistor g-s capacitance	330aF	330aF
$V_b$	Applied bias voltage	670mV	96AmV

In the absence of wire parasitics and process variations, the bias voltage range for the implementation of a BUFFER gate can be obtained from Table 1. In [2], we reported the numerical values of bias voltages for different gates. For the BUFFER gate, under today's technology and advanced technology, the voltage ranges are 552–788 and 70–121 mV, respectively [2]. To maximize the noise margin (NM), we would choose the midpoint of the interval,  $V_b = 670$  mV for today's CRAM and  $V_b = 96$  mV for advanced CRAM, to implement the BUFFER. This voltage is applied through drivers at the edge of the CRAM array, where each driver has a resistance  $R_D$ . The CRAM rows in Fig. 2 are numbered from 1 (the nearest row to the driver) to  $N_{row}$  (the farthest row). When parasitics are accounted for, it can be seen that the path to row 1 encounters the fewest parasitics and that the path to row  $N_{row}$  the most, due to IR drop along the line. Thus, the voltage  $V_b = 670$  mV in today's CRAM (and  $V_b = 96$  mV in advanced CRAM) may not be significantly changed as it reaches the first row, but the voltage at row  $N_{row}$  may be significantly degraded.

Given the fixed voltage range (552–788 mV for today's CRAM and 70–121 mV for advanced CRAM) within which the BUFFER operates correctly, the entire array will operate correctly when the BSL voltage for Row 1 is at the maximum  $V_b$  value and the BSL voltage for Row  $i$  is at the minimum allowable  $V_b$  for the BUFFER. Thus, the maximum allowable voltage drop is the difference between the maximum and minimum  $V_b$ , i.e., 226 mV in today's CRAM and 51 mV

**TABLE 3.** IR drop differential between the BSL voltage for the first row and the last row, and the RC delay of the transition.

# rows	Today's CRAM		Advanced CRAM	
	IR drop	RC delay	IR drop	RC delay
64	5.8mV	87fs	0.2mV	52fs
128	22.4mV	346fs	0.6mV	210fs
256	82.3mV	1.3ps	2.3mV	798fs
512	250.0mV	4.1ps	8.5mV	3.1ps
1024	507.9mV	10.3ps	38.0mV	10.6ps
2048	650.3mV	18.4ps	75.6mV	26.1ps

in advanced CRAM for BUFFER, and a similarly calculated value from Table 1 for any other gate. In practice, the drop must be even smaller to allow for NMs.

We consider six CRAM array configurations, each with a different number of rows, and use Table 3 to show the degradation of  $V_b$  as it reaches the farthest row for each of these configurations. If each row performs an identical operation in the worst case, it should carry an equal current  $I_{row}$  and the total voltage drop to the last row is

$$nI_{row}R_y + (n-1)I_{row}R_y + \dots + I_{row}R_y = n(n+1)/2 I_{row}R_y$$

i.e., the IR drop increases quadratically with the number of rows. For the 64-row array (in both CRAMs), Table 3 shows that this IR drop is not large, but for arrays with 256 rows and larger in today's CRAM (and for 2048 rows in advanced CRAM), the IR drop is a significant fraction of  $V_b$ . The quadratic trend is seen between the first few rows, but the trend becomes subquadratic in the last few rows; this is due to the high voltage drop, the current supplied to that row is significantly less than supplied to the first row (e.g., for  $N_{row} = 2024$ , the voltage level at the last row is about 20 mV for today's CRAM (and 30 mV for advanced CRAMA), far less than  $V_{min}$  for a buffer). This invalidates the assumption in the abovementioned derivation that an equal current of  $I_{row}$  is supplied to each row.

Next, we compute the impact of RC parasitics on the CRAM delay. Defining the transition time as the time to 90% of the final value, Table 3 shows that this time is negligible in comparison with the nanosecond-range MTJ switching time. Thus, wire parasitics do not impact the delay but only the IR drop.

#### IV. LAYOUT MODELING

The key parameters that affect the IR drop are given as follows:

- 1) number of rows, for reasons illustrated in Table 3;
- 2) transistor resistance  $R_T$ , which is in series with the MTJ resistance; a higher value reduces the NM (the value of  $R_T$  can be reduced by increasing the transistor width, which may increase the cell area);
- 3) cell area,  $A_{cell} = W_{cell}L_{cell}$  (where  $W_{cell}$  and  $L_{cell}$  are the cell width and length, respectively), which impacts the BSL and LL lengths, thus affecting IR drop;
- 4) cell aspect ratio,  $AR_{cell} = (W_{cell}/L_{cell})$ , which determines the BSL and LL lengths (a larger  $AR_{cell}$  makes the BSLs longer, causing increasing parasitics on them, while shortening LLs and reducing their parasitics);
- 5) configuration of BSLs and LLs, whose resistance can be reduced using a multimetal layer structure and whose length and width depend on other parameter choices.

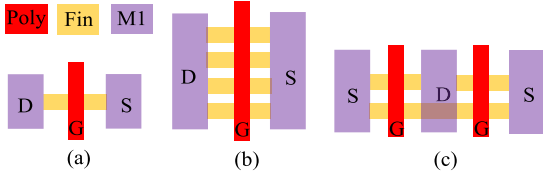


**FIGURE 3.** Layout of FinFET devices with (a) one fin and one finger, (b) four fins and one finger, and (c) two fins and two fingers.

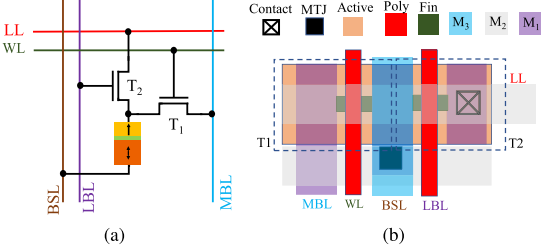


**FIGURE 4.** CRAM cell. (a) Schematic. (b) Layout.

### A. LAYOUT OF A CRAM CELL

Designing an STT-MRAM with a FinFET access transistor can reduce the cell area and improve leakage power and reliability [10]. The design in this article is based on ASAP 7-nm Predictive PDK [11]. Fig. 3(a) shows the layout of a FinFET using a single fin. By applying the proper voltage to the gate (G), the current flows from drain (D) to the source (S) through the fin. By increasing the number of fins, the ON current increases and the drain–source resistance of the of FinFET decreases, at the cost of an increase in FinFET area. Such transistors can be drawn in multiple ways: a  $4 \times$  FinFET is shown in Fig. 3(b) with four fins, or alternatively, in Fig. 3(c), using two fingers with two fins each. For the same transistor ON resistance, one can change the aspect ratio of the FinFET device by varying the numbers of fins and fingers.

Fig. 4 shows the schematic and layout of the CRAM cell using a one-fin one-finger FinFET. The source of T1 is connected to MBL and M1 is allocated for MBL routing; the poly in T1 is used for WL; the drain of T1 is connected to the MTJ, which is physically placed between M2 and M3. For T2, the drain is connected to LL, the poly is used locally for LBL, and the source is connected to the MTJ. In the layout, a horizontal M2 stripe is used for LL routing, and a vertical M3 stripe is used for BSL. Larger transistor sizes can be achieved by using multiple fins and fingers for each transistor, changing the cell dimension in the vertical and horizontal directions.

### B. LAYOUT OF THE CRAM ARRAY

The CRAM cell can be tessellated into an array. Fig. 5 shows the layout of four adjacent CRAM cells ( $2 \times 2$ ), again using a one-fin one-finger FinFET, under ASAP7 design rules [11], [12]. For example, the minimum allowable active width is 27 nm; the poly length and pitch are 20 and 54 nm, respectively; the minimum active-to-active distance in our design can be 54 nm: under these constraints, the size of the smallest one-fin, one-finger CRAM cell is 108 nm  $\times$  189 nm. The addition of each fin increases the cell width (vertical dimension) by 27 nm, keeping the cell length (horizontal

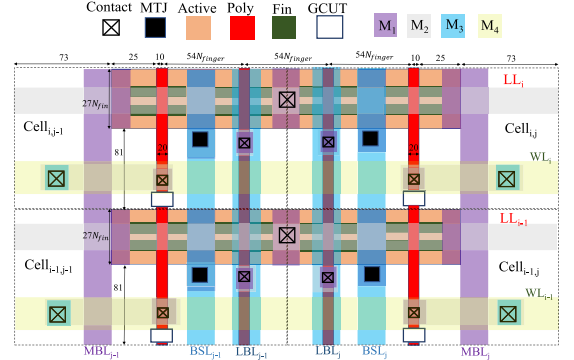


**FIGURE 5.** Layout of four adjacent CRAM cells in ASAP7.

dimension) fixed, while adding each finger increases the cell length by 108 nm, leaving the width fixed. The width and length for a cell with  $N_{\text{fin}}$  fins and  $N_{\text{finger}}$  fingers are

$$W_{\text{cell}} = 108 + 27(N_{\text{fin}} - 1) \quad (4)$$

$$L_{\text{cell}} = 189 + 162(N_{\text{finger}} - 1). \quad (5)$$

### C. IMPACT OF LAYOUT CHOICES ON

( $A_{\text{cell}}$ ,  $AR_{\text{cell}}$ , and  $R_T$ )

The choice of  $W_{\text{cell}}$  and  $L_{\text{cell}}$  can impact the cell area,  $A_{\text{cell}} = W_{\text{cell}} \times L_{\text{cell}}$ , and the cell aspect ratio,  $AR_{\text{cell}} = W_{\text{cell}}/L_{\text{cell}}$ . From (4) and (5), the following trends can be inferred as the numbers of fins and fingers are changed.

- 1) By increasing  $N_{\text{fin}}$  and  $N_{\text{finger}}$ , both  $W_{\text{cell}}$  and  $L_{\text{cell}}$  increase, increasing  $A_{\text{cell}}$ .
- 2) For fixed  $N_{\text{fin}}$ , the largest  $AR_{\text{cell}}$  has the lowest  $L_{\text{cell}}$ , i.e.,  $N_{\text{finger}} = 1$ . If we fix  $N_{\text{finger}}$ , then by increasing  $N_{\text{fin}}$ ,  $W_{\text{cell}}$  increases; thus,  $AR_{\text{cell}}$  increases.

Next, we study the impact of the numbers of fins and fingers on the transistor resistance,  $R_T$ , for both advanced CRAM and today's CRAM. We apply the nominal voltage of ASAP7 (0.7 V) to the FinFET gate, and for this value of gate-to-source voltage  $V_{\text{gs}}$ , we use the transistor  $I$ - $V$  curve to determine the resistance corresponding to the drain-to-source current  $I_{\text{ds}} = I_c$  (Table 7) required to switch an MTJ. Today's MTJ requires larger  $I_c$  than the advanced MTJ; hence, for the same  $N_{\text{fin}}$  and  $N_{\text{finger}}$ ,  $R_T$  is larger for today's CRAM. The  $N_{\text{fin}} = N_{\text{finger}} = 1$  case can deliver  $I_c$  for the advanced MTJ, but not for today's MTJ; larger sizes must be used for the latter. As expected, as  $N_{\text{fin}}$  and  $N_{\text{finger}}$  are increased,  $R_T$  reduces.

### D. METAL LAYER CONFIGURATIONS AND SPECIFICATIONS

As seen in Section III, parasitics in the BSLs and LLs play a large part in limiting the allowable size of the CRAM array. To overcome this, we use a multimetal layer architecture for BSLs and LLs, shown in Fig. 6 for the four adjacent CRAM cells of Fig. 5. Here, metal layers M3, M5, M7, and M9 are allocated to the BSLs, and M2 and M4 are allocated to LLs, with vias connecting each type of line across layers. The interconnect specifications—the metal thickness ( $t_M$ ), resistivity ( $\rho_M$ ), minimum spacing ( $S_{\text{min}}$ ), minimum width ( $W_{\text{min}}$ ), and via parameters—are taken from [11] and [12].



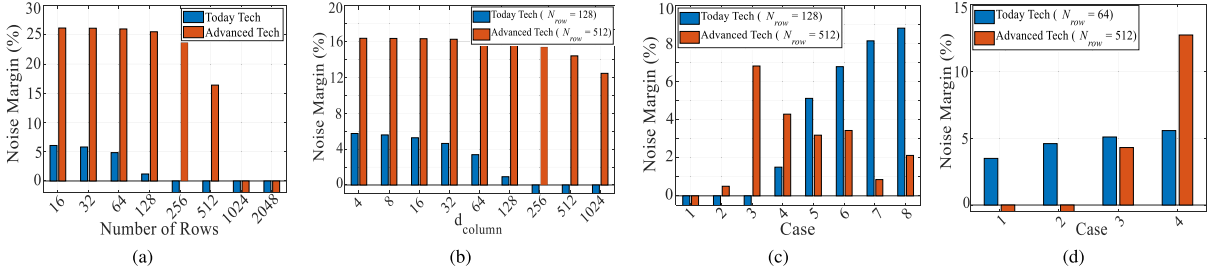


FIGURE 9. NM for an AND gate in today's and advanced CRAM, varying (a)  $N_{\text{row}}$ , (b)  $d_{\text{column}}$ , (c)  $R_T$ , and (d)  $AR_{\text{cell}}$ .

## 2) EFFECT OF $d_{\text{column}}$

By increasing the relative distance between the input columns and the output column ( $d_{\text{column}}$ ), the parasitics associated with the LL in each row ( $R_x$ ) increase. Fig. 9(b) shows NM for different cases with different  $d_{\text{column}}$  values in today's and advanced CRAMs. For the advanced CRAM, the value of  $d_{\text{column}}$  does not affect NM significantly for the shown values because the LL parasitic resistance,  $R_x \ll R_{\text{MTJ}}$ , the MTJ resistance to which it is connected in series. For today's CRAM, only  $d_{\text{column}} \leq 64$  provide a positive NM because  $R_x$  is comparable with  $R_T$  for today's MTJs. High values of  $d_{\text{column}}$  create a large drop across the parasitics, causing  $V_b$  to be infeasible.

Similar trends are seen for the BUFFER, where the range of a copy operation is limited using today's CRAM. Thus, copy operations over large distances must be performed in multiple steps, adding to the energy and computation time.

## 3) EFFECT OF $R_T$

To analyze the effect  $R_T$ , we must consider that  $A_{\text{cell}}$  changes accordingly if we vary  $R_T$ . The choice of  $R_T$  can affect NM through two mechanisms: 1) directly, since a reduction in  $R_T$  increases the noise margin for an array of constant size and 2) indirectly, since a reduction in  $R_T$  increases the cell size, and hence the array size, thereby increasing line parasitics  $R_x$  and  $R_y$ .

In Table 4, we present eight cases where  $R_T$  gradually decreases from case 1 to case 8. For both advanced and today's CRAMs, case 1 has the smallest  $R_T$  (the largest  $A_{\text{cell}}$ ), and case 8 has the largest  $R_T$  (the smallest  $A_{\text{cell}}$ ). We choose  $W_{\text{cell}}$  and  $L_{\text{cell}}$  so that the  $AR_{\text{cell}}$  values are roughly constant (it is not possible to ensure equality since  $R_T$  is changed over a discrete space by altering  $N_{\text{fin}}$  and  $N_{\text{finger}}$ ). We set  $N_{\text{row}}$  to 128 and 512, respectively, for today's and advanced technologies and set  $d_{\text{column}} = 10$  for both cases.

Fig. 9(c) shows the NM for each of these cases. For today's technology, large  $R_T$  values (cases 1–3) cause negative NM, as in these cases,  $R_T$  values are comparable with today's MTJ resistances, and reducing  $R_T$  further improves NM. The direct mechanism is dominant here, and reducing  $R_T$  improves NM monotonically. In contrast, for advanced MTJs, there is a nonmonotone relationship as  $R_T$  is reduced. At first, NM improves due to the first mechanism, and then, it worsens due to the second mechanism. Part of the nonmonotonicity (e.g., between cases 5 and 6) can be attributed to the fact that  $AR_{\text{cell}}$  is not strictly constant in Table 4 (in fact, for case 1, for the advanced CRAM, the FinFET has  $N_{\text{fin}} = N_{\text{finger}} = 1$ , and the corresponding  $AR = 0.57$  is the only option). Over the eight choices, one can choose case 3 as the optimal point that provides the best NM.

TABLE 4. Analyzing the effect of  $R_T$ .

	Today's CRAM			Advanced CRAM		
	$R_T$	$A_{\text{cell}}$	$AR_{\text{cell}}$	$R_T$	$A_{\text{cell}}$	$AR_{\text{cell}}$
1	5.99K $\Omega$	0.020 $\mu\text{m}^2$	0.4	5.73K $\Omega$	0.020 $\mu\text{m}^2$	0.57
2	1.72K $\Omega$	0.038 $\mu\text{m}^2$	0.31	2.87K $\Omega$	0.029 $\mu\text{m}^2$	0.40
3	1.04K $\Omega$	0.047 $\mu\text{m}^2$	0.38	1.90K $\Omega$	0.038 $\mu\text{m}^2$	0.31
4	0.76K $\Omega$	0.058 $\mu\text{m}^2$	0.31	0.95K $\Omega$	0.047 $\mu\text{m}^2$	0.38
5	0.49K $\Omega$	0.067 $\mu\text{m}^2$	0.37	0.63K $\Omega$	0.057 $\mu\text{m}^2$	0.41
6	0.36K $\Omega$	0.082 $\mu\text{m}^2$	0.43	0.48K $\Omega$	0.067 $\mu\text{m}^2$	0.38
7	0.29K $\Omega$	0.096 $\mu\text{m}^2$	0.36	0.35K $\Omega$	0.081 $\mu\text{m}^2$	0.43
8	0.23K $\Omega$	0.110 $\mu\text{m}^2$	0.42	0.23K $\Omega$	0.110 $\mu\text{m}^2$	0.42

TABLE 5. Analyzing the effect of  $AR_{\text{cell}}$ .

	Today's CRAM			Advanced CRAM		
	$AR_{\text{cell}}$	$A_{\text{cell}}$	$R_T$	$AR_{\text{cell}}$	$A_{\text{cell}}$	$R_T$
1	0.80	0.058 $\mu\text{m}^2$	0.59K $\Omega$	1.14	0.041 $\mu\text{m}^2$	1.14K $\Omega$
2	0.54	0.066 $\mu\text{m}^2$	0.49K $\Omega$	0.60	0.044 $\mu\text{m}^2$	0.95K $\Omega$
3	0.38	0.069 $\mu\text{m}^2$	0.49K $\Omega$	0.38	0.047 $\mu\text{m}^2$	0.95K $\Omega$
4	0.26	0.069 $\mu\text{m}^2$	0.59K $\Omega$	0.21	0.055 $\mu\text{m}^2$	1.14K $\Omega$

## 4) EFFECT OF $AR_{\text{cell}}$

We now vary  $AR_{\text{cell}}$  by changing  $N_{\text{fin}}$  and  $N_{\text{finger}}$  while keeping  $R_T$  and  $A_{\text{cell}}$  relatively fixed. As stated before, we set  $N_{\text{row}}$  to 128 and 512, respectively, for today's CRAM and the advanced CRAM;  $d_{\text{column}} = 10$ , and  $R_T$  and  $A_{\text{cell}}$  are kept roughly constant, to the extent possible in the discrete space of  $N_{\text{fin}}$  and  $N_{\text{finger}}$ .

Fig. 9(d) shows the results for the four cases Table 5. Cases with smaller  $AR_{\text{cell}}$ , which have shorter BSLs with lower parasitic resistances ( $R_y$ ), have a larger NM value. Thus, an appropriate choice of  $AR_{\text{cell}}$  can improve the performance of the CRAM without area overhead. For example, in advanced CRAM, the NM for case 1, with the smallest  $AR_{\text{cell}}$ , is negative, but NM improves as  $AR_{\text{cell}}$  is increased.

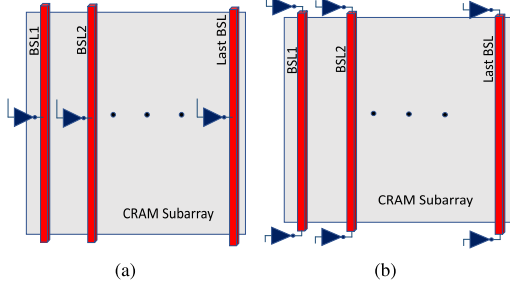
## 5) OPTIMAL DESIGN FOR EACH GATE

Table 6 evaluates the implementations of three types of arrays using both today's and advanced CRAMs with various degrees of versatility: Array 1 implements a basic set of combinational logic gates (INV, BUFFER, AND/NAND, and OR/NOR), Array 2 adds the MAJ3 and MAJ3 gates to this set, and Array 3 further adds MAJ5 and MAJ5. It is easily seen that for more versatile arrays, the array size is more constrained. The improvement from today's CRAM to the advanced CRAM is also visible: for example, today's CRAM cannot implement Array 3, regardless of array size [2].

To obtain the largest allowable size of  $N_{\text{row}}$ , we change the locations of the BSL drivers. Compared with the previous

**TABLE 6. Optimal design options for arrays with different functionalities.**

		$N_{fin},$ $N_{finger}$	$R_T$ (K $\Omega$ )	$A_{cell}$ ( $\mu m^2$ ), $AR_{cell}$	$N_{row},$ $d_{column}$	Subarray Size
1	Advanced	4, 4	0.357	0.127, 0.280	512, 512	32KB
	Today's	5, 7	0.113	0.251, 0.186	128, 64	1024KB
2	Advanced	2, 6	0.476	0.135, 0.134	256, 256	4KB
	Today's	4, 9	0.101	0.281, 0.127	128, 16	256KB
3	Advanced	3, 9	0.171	0.267, 0.098	256, 64	2KB
	Today's	-	-	-	-	-


**FIGURE 10. Increasing  $N_{row}$  by inserting (a) 2x drivers in the middle of the array and (b) two 1x drivers at either end.**

analysis where a driver was placed at one end of the array, we effectively double  $N_{row}$  by using a 2x driver in the middle of the array or by using two 1x drivers at either end of the array (see Fig. 10). The area overheads are modest.

Note that the constraint on  $N_{row}$  limits the array size but not the CRAM size; the overall CRAM consists of a tiled set of arrays, each with  $N_{row}$  rows, and all controlled by the same set of control signals. The choice of  $d_{column}$ , however, does not constrain the tile size but merely the computation distance. If the operands of a computation are at a distance  $> d_{column}$  from each other, then they must be copied to new cells that are within the  $d_{column}$  limit. This is often not a problem; all the computations shown in [2] lie within the  $d_{column}$  constraint listed in Table 6. For this reason, practically,  $N_{row}$  is much more constraining than  $d_{column}$ .

## VII. CONCLUSION

We have presented a methodology based on actual layout considerations for analyzing the parasitic effects in STT-CRAM. We have demonstrated that interconnect parasitics have a significant effect on CRAM performance and have developed a comprehensive model for analyzing this impact. Using this methodology, we have developed guidelines for the array size,  $N_{row}$ , and the maximum distance between the columns for an operation. We show that for both today's and advanced technologies, CRAM cell layouts with smaller aspect ratios are desirable, as this helps control critical BSL parasitics. Reducing access transistor resistance is important for today's technology but is not a significant factor for advanced technologies. For the SHE-CRAM [13], a similar analysis shows that interconnect parasitics are not significant as the current values are much smaller.

## APPENDIX

### A. THEVENIN MODEL FOR ONE-INPUT GATES

We derive the recursive expressions for  $R_{th}$  and  $\alpha_{th}$  for each row in the CRAM array. The exposition here derives an expression for  $V_{th}$ , and  $\alpha_{th}$  is trivially obtained from (6).

Within the footprint area of a CRAM cell, we define  $R_y$ ,  $R_x$ , and  $R_{Via}$  as lumped resistances for BSL segment, LL segment, and vias, respectively. Fig. 11 shows the equivalent simplified circuit of the path for the implementation of BUFFER (or NOT) gates on CRAM rows. Row  $i$  is separated from its predecessor by resistances  $R_y$  at each end and is connected through  $R_{Via}$  to an input MTJ cell, represented by  $R_i^{MTJ1}$  and  $R_T$ . The input cell is connected to the output cell,  $d_{column}$  rows away, through a resistance  $R_x$ , and the output cell is represented by a transistor resistance  $R_T$  in series with a preset MTJ resistance,  $R_{MTJ2}$ . The resistances in the last row are rearranged to create a two-port structure consisting of the MTJ resistances so that the rest of the network can be modeled using the Thevenin equivalents ( $R_{th}$  and  $V_{th}$ ).

Depending on the states of the inputs in different rows, which are application-dependent, the resistances of the MTJs, and hence the Thevenin parameters, change and typically vary in different rows. To provide a robust design, we consider the worst case in which the combination of the values of inputs in different rows results in the worst voltage drop across the MTJs of the last row. This worst case corresponds to the worst case current, which is drawn when all inputs MTJs in all rows are in the parallel state, creating  $N_{row} - 1$  paths with the lowest possible resistance possible between the input and output BSLs.

As explained in Section IV-D, the BSL and LL lines have a multilayer structure. The metal layer resistances are considered to be in parallel, and  $R_y$  and  $R_x$  are expressed by

$$R_y^{-1} = R_{M_3}^{-1} + R_{M_5}^{-1} + R_{M_7}^{-1} + R_{M_9}^{-1} \quad (11)$$

$$R_x^{-1} = d_{column}^{-1} (R_{M_2}^{-1} + R_{M_4}^{-1}) \quad (12)$$

where  $d_{column}$  is the number of wire segments between the input and output columns. The resistance  $R_{M_k}$  is given by:  $R_{M_k} = (\rho_{M_k} L_{M_k}) / (t_{M_k} W_{M_k})$ , where  $\rho_{M_k}$ ,  $L_{M_k}$ ,  $t_{M_k}$ , and  $W_{M_k}$  are, respectively, the resistivity, length, thickness, and width in metal layer  $k$ . The equivalent resistance of the vias,  $R_{Via}$ , depends on the configuration of the CRAM cell; a larger CRAM cell contains more vias in its footprint area, as a consequence of which  $R_{Via}$  is smaller. The number of vias between two metal layers in the footprint area of a CRAM cell can be calculated based on the via characteristics in Table 9 (see the Supplementary Material), as the parallel resistance of the available number of vias.

The abovementioned equivalent resistive introduces a minor simplification because the parallel wires do not coincide at a single point, but the vias are a small distance apart. HSPICE simulations show less than 0.5% error.

To calculate  $R_{th}$  and  $V_{th}$ , we derive recursive expressions. For conciseness, we define the resistance  $R_{row_i}$  of row  $i$  as

$$R_{row_i} = 2(R_{Via} + R_T) + R_x + R_i^{MTJ1} + R_{MTJ2}. \quad (13)$$

The input logic value depends on the application, i.e.,  $R_i^{MTJ1}$  can be either  $R_P$  or  $R_{AP}$ . For each gate, the output resistance is a known preset value; for a Buffer (NOT) gate implemented across all rows, the preset is 1 (0). Therefore,  $R_{MTJ2}$  for the Buffer and NOT gates are  $R_{AP}$  and  $R_P$ , respectively.

We can obtain  $R_{th}$ , using the notations in Fig. 11(b), as

$$R_{th} = 2(R_y + R_{Via}) + R_x + R_{N_{row}-1} \quad (14)$$

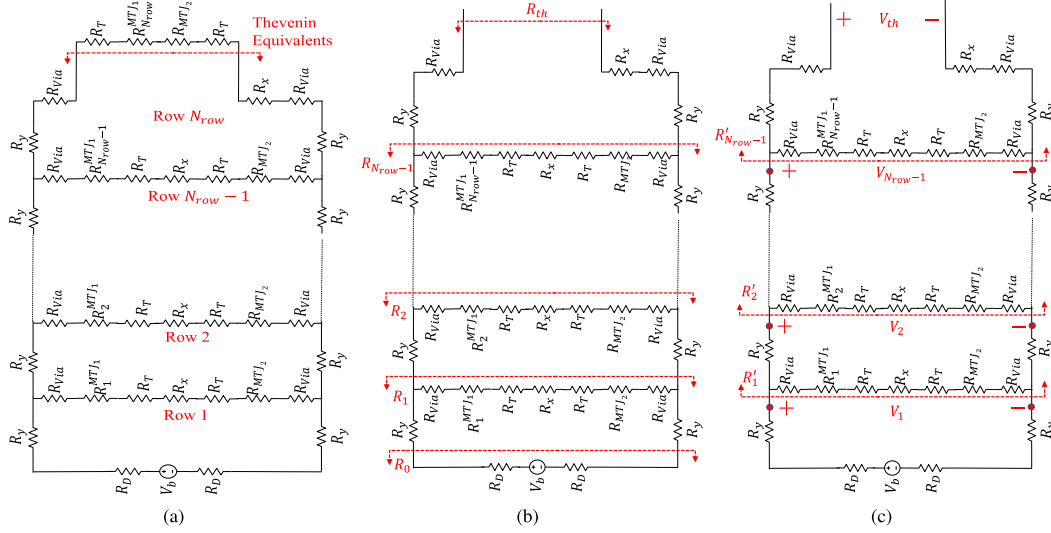


**FIGURE 11.** (a) Circuit model for one-input gates, showing the observation point for calculating Thevenin equivalent. Notations used in the chain of rows for defining (b) Thevenin resistance ( $R_{th}$ ) and (c) Thevenin voltage ( $V_{th}$ ).

where  $R_{N_{row}-1}$  is calculated using the recursive expression

$$R_i = \frac{R_{row_i}(R_{i-1} + 2R_y)}{R_{row_i} + R_{i-1} + 2R_y}. \quad (15)$$

The base case corresponds to the driver row that precedes the first row and is  $R_0 = 2R_D$ , as shown in Fig. 11(a).

To compute  $V_{th}$ , as shown in Fig. 11(c), we first compute the intermediate variable  $R'_j$ , which corresponds to the effective downstream resistance (away from the source) seen from node  $j$ . The computation proceeds in a recursive fashion from the last row toward the first as

$$R'_{j-1} = \frac{R_{row_{j-1}}(R'_j + 2R_y)}{R_{row_{j-1}} + R'_j + 2R_y} \quad (16)$$

with the base case  $R'_{N_{row}-1} = R_{row_{N_{row}-1}}$ .

Having computed  $R'_j$ , we may now compute  $V_{th} = V_{N_{row}}$  using a recursive computation on  $V_i$

$$V_j = \frac{R'_j}{2R_y + R'_j} V_{j-1} \quad (17)$$

in which  $2 \leq j \leq N_{row} - 1$  and the base case is

$$V_1 = \frac{R'_1}{R'_1 + 2R_y + 2R_D} V_b. \quad (18)$$

## B. THEVENIN MODEL FOR N-INPUT GATES

The one-input model can easily be extended for the case where the number of inputs  $N > 1$ . For this case, we have  $N$  columns of input MTJs that connect to an output MTJ in each row; the worst case corresponds to the scenario where all inputs are adjacent to each other and  $d_{column}$  columns away from the output. As a simplification, we assume that all units are equally far and that the resistance to the output for each is  $R_x$ ; this is reasonable because the horizontal resistance between the adjacent columns is negligible. In this case, in column  $i$ ,  $N$  parallel structures, each consisting of series connections of  $R_y$ ,  $R_{via}$ ,  $R_i^{MTJ1}$ , and  $R_T$ , connect through  $R_x$

to the output cell, modeled as a series connection of  $R_T$  and  $R_{MTJ2}$ . We generalize (13) to

$$R_{Row_i} = \left(1 + \frac{1}{N}\right) (R_{via} + R_T) + R_x + \frac{R_i^{MTJ1}}{N} + R_{MTJ2}. \quad (19)$$

Proceeding similar to the one-input case, we generalize (14) to compute  $R_{th}$  as

$$R_{th} = \left(1 + \frac{1}{N}\right) (R_y + R_{via}) + R_x + R_{N_{row}-1} \quad (20)$$

where  $R_{N_{row}-1}$  can be obtained using the recursion

$$R_i = \frac{R_{Row_i}(R_{i-1} + \left(1 + \frac{1}{N}\right) R_y)}{R_{Row_i} + R_{i-1} + \left(1 + \frac{1}{N}\right) R_y} \quad (21)$$

where  $1 \leq i \leq N_{row} - 1$  and the base case is  $R_1 = \left(1 + \frac{1}{N}\right) R_D$ , corresponding to the fact that each input line is driven by a source  $V_b$  with a series resistance  $R_D$  to the first via.

Similarly, one can recursively compute  $V_{th}$ . Analogously to (16), we first compute  $R'_j$  recursively, from the last row to the first, as

$$R'_{j-1} = \frac{R_{Row_{j-1}}(R'_j + \left(1 + \frac{1}{N}\right) R_y)}{R_{Row_{j-1}} + R'_j + \left(1 + \frac{1}{N}\right) R_y} \quad (22)$$

where the base case is  $R'_{N_{row}-1} = R_{Row_{N_{row}-1}}$ .

We can then compute  $V_{th} = V_{N_{row}}$  recursively using the following recursion for  $V_j$ :

$$V_j = \frac{R'_j}{\left(1 + \frac{1}{N}\right) R_y + R'_j} V_{j-1} \quad (23)$$

in which  $2 \leq j \leq N_{row} - 1$  and the base case is

$$V_1 = \frac{R'_1}{R'_1 + \left(1 + \frac{1}{N}\right) R_y + \left(1 + \frac{1}{N}\right) R_D} V_b. \quad (24)$$

## REFERENCES

- [1] J.-P. Wang and J. D. Harms, "General structure for computational random access memory (CRAM)," U.S. Patent 9224447 B2, Dec. 29, 2015. [Online]. Available: <https://www.google.com/patents/US9224447>
- [2] M. Zabihi, Z. I. Chowdhury, Z. Zhao, U. R. Karpuzcu, J.-P. Wang, and S. S. Sapatnekar, "In-memory processing on the spintronic CRAM: From hardware design to application mapping," *IEEE Trans. Comput.*, vol. 68, no. 8, pp. 1159–1173, Aug. 2019.
- [3] M. Zabihi et al., "True in-memory computing with the CRAM: From technology to applications," in *Proc. Great Lakes Symp. VLSI (GLSVLSI)*, 2019, p. 379.
- [4] Y. Jeong, M. A. Zidan, and W. D. Lu, "Parasitic effect analysis in memristor-array-based neuromorphic systems," *IEEE Trans. Nanotechnol.*, vol. 17, no. 1, pp. 184–193, Jan. 2018.
- [5] N. M. G., F. Lalchandama, K. Datta, and I. Sengupta, "Modelling and simulation of non-ideal MAGIC NOR gates on memristor crossbar," in *Proc. 8th Int. Symp. Embedded Comput. Syst. Design (ISED)*, Dec. 2018, pp. 124–128.
- [6] J.-P. Wang et al., "A pathway to enable exponential scaling for the beyond-CMOS era," in *Proc. 54th Annu. Design Autom. Conf. (DAC)*, 2017, pp. 1–6.
- [7] J. Kim et al., "Spin-based computing: Device concepts, current status, and a case study on a high-performance microprocessor," *Proc. IEEE*, vol. 103, no. 1, pp. 106–130, Jan. 2015.
- [8] Z. Chowdhury et al., "Efficient in-memory processing using spintronics," *IEEE Comput. Archit. Lett.*, vol. 17, no. 1, pp. 42–46, Jan. 2018.
- [9] A. Hirohata et al., "Roadmap for emerging materials for spintronic device applications," *IEEE Trans. Magn.*, vol. 51, no. 10, pp. 1–11, Oct. 2015.
- [10] A. Shafaei, Y. Wang, and M. Pedram, "Low write-energy STT-MRAMs using FinFET-based access transistors," in *Proc. IEEE 32nd Int. Conf. Comput. Design (ICCD)*, Oct. 2014, pp. 374–379.
- [11] L. T. Clark et al., "ASAP7: A 7-nm finFET predictive process design kit," *Microelectron. J.*, vol. 53, pp. 105–115, Jul. 2016.
- [12] L. T. Clark, V. Vashishtha, D. M. Harris, S. Dietrich, and Z. Wang, "Design flows and collateral for the ASAP7 7nm FinFET predictive process design kit," in *Proc. IEEE Int. Conf. Microelectron. Syst. Edu. (MSE)*, May 2017, pp. 1–4.
- [13] M. Zabihi et al., "Using spin-Hall MTJs to build an energy-efficient in-memory computation platform," in *Proc. 20th Int. Symp. Qual. Electron. Design (ISQED)*, Mar. 2019, pp. 52–57.
- [14] G. Jan et al., "Demonstration of fully functional 8Mb perpendicular STT-MRAM chips with sub-5ns writing for non-volatile embedded memories," in *Symp. VLSI Technol. (VLSI-Technol.): Dig. Tech. Papers*, Jun. 2014, pp. 1–2.
- [15] H. Maehara et al., "Tunnel Magnetoresistance above 170% and resistance-area product of  $1 \Omega (\mu\text{m})^2$  attained by in situ annealing of ultra-thin MgO tunnel barrier," *Appl. Phys. Express*, vol. 4, no. 3, Mar. 2011, Art. no. 033002.
- [16] H. Noguchi et al., "7.5 A 3.3 ns-access-time 71.2  $\mu\text{W}/\text{MHz}$  1Mb embedded STT-MRAM using physically eliminated read-disturb scheme and normally-off memory architecture," in *Proc. IEEE Int. Solid-State Circuits Conf.*, Feb. 2015, pp. 1–3.

**MASOUD ZABIHI** received the B.Sc. degree in electrical engineering from the University of Tabriz, and the M.S. degree in electrical engineering from the Sharif University of Technology, Iran. He is currently pursuing the Ph.D. degree with the University of Minnesota, Minneapolis, MN, USA.

His research interests include in-memory computing, emerging memory technologies, and VLSI design automation.

**ARVIND K. SHARMA** received the Ph.D. degree from IIT Roorkee, Roorkee, India, in 2018.

He is currently a Post-Doctoral Associate at the Department of Electrical and Computer Engineering, University of Minnesota, Minneapolis, MN, USA. His current research interests include device physics, circuit device interaction, layout automation, and variability-aware circuit design.

**MEGHNA G. MANKALALE** received the B.E. degree from Visvesvaraya Technological University, India, in 2007, and the Ph.D. degree from the Department of Electrical and Computer Engineering, University of Minnesota, Minneapolis, MN, USA, in 2020.

She has worked as a Research and Development Engineer at the Electronic Design Automation Group, IBM, India, from 2007 to 2013. She currently works as a Sr. R&D Engineer at Synopsys.

**ZAMSHED IQBAL CHOWDHURY** (Member, IEEE) is currently pursuing the Ph.D. degree with the Department of Electrical and Computer Engineering, University of Minnesota, Minneapolis, MN, USA.

He is a Faculty Member (on leave) at Jahangirnagar University, Bangladesh. His primary research interests include emerging non-volatile memory technologies, application-specific hardware design, and computer performance analysis.

**ZHENGYANG ZHAO** received the B.S. degree in electrical engineering from Xi'an Jiaotong University, China. He is currently pursuing the Ph.D. degree in electrical engineering with the University of Minnesota, Minneapolis, MN, USA.

His research focuses on the development of spintronic devices for memory and computing applications.

**SALONIK RESCH** received the bachelor's degree in computer engineering from the University of Minnesota, Minneapolis, MN, USA, in 2016, where he is currently pursuing the Ph.D. degree.

His research interests include processing-in-memory, intermittent computing, and quantum computing.

**ULYA R. KARPUZCU** received the M.S. and Ph.D. degrees in computer engineering from the University of Illinois, Urbana-Champaign, IL, USA.

She is currently an Associate Professor with the Department of Electrical and Computer Engineering, University of Minnesota, Minneapolis, MN, USA. Her research interests span the impact of technology on computing, energy-efficient computing, application domain specialized architectures, approximate computing, and computing at ultra-low voltages.

**JIAN-PING WANG** (Fellow, IEEE) received the Ph.D. degree in magnetism from the Institute of Physics, CAS, in 1995. He finished his post-doctoral training from the National University of Singapore in 1996.

He was the Director of the Center for Spintronic Materials, Interfaces and Novel Architectures (C-SPIN). He is currently the Robert F. Hartmann Chair and a Distinguished McKnight University Professor of Electrical and Computer Engineering at the University of Minnesota. He is also the Director of the Center for Spintronic Materials for Advanced Information Technology (SMART), one of two SRC/NIST nCORE research centers.

Dr. Wang received the INSIC Technical Award in 2006 and the SRC Technical Excellence Award in 2019.

**SACHIN S. SAPATNEKAR** (Fellow, IEEE) received the B.Tech. degree from IIT Bombay, the M.S. degree from Syracuse University, and the Ph.D. degree from the University of Illinois.

He is on the faculty at the University of Minnesota, Minneapolis, MN, USA, where he holds the Distinguished McKnight University Professorship and the Robert and Marjorie Henle Chair in the Department of Electrical and Computer Engineering.

Dr. Sapatnekar is a fellow of the ACM. He has received eight conference Best Paper Awards, a Best Poster Award, two ICCAD 10-year Retrospective Most Influential Paper Awards, the SRC Technical Excellence Award, and the SIA University Research Award.

• • •